EFDA–JET–PR(06)28

C.F. Maggi, R.J. Groebner, N. Oyama, R. Sartori, L.D. Horton, A.C.C. Sips, W. Suttrop and ASDEX Upgrade Team, T. Leonard, T.C. Luce, M.R. Wade and DIII-D Team, Y. Kamada, H. Urano and JT-60U Team, Y. Andrew, C. Giroud, E. Joffrin, E. de la Luna and EFDA-JET Contributors* for the Pedestal and Edge Physics and the Steady State Operation Topical Groups of the ITPA

Characteristics of the H-mode Pedestal in Improved Confinement Scenarios in ASDEX Upgrade, DIII-D, JET and JT-60U

Characteristics of the H-mode Pedestal in Improved Confinement Scenarios in ASDEX Upgrade, DIII-D, JET and JT-60U

C.F. Maggi[1], R.J. Groebner[2], N. Oyama[3], R. Sartori[4], L.D. Horton[1], A.C.C. Sips[1], W. Suttrop[1] and ASDEX Upgrade Team, T. Leonard[2], T.C. Luce[2], M.R. Wade[2] and DIII-D Team, Y. Kamada[3], H. Urano[3] and JT-60U Team, Y. Andrew[5], C. Giroud[5], E. Joffrin[6], E. de la Luna[7] and EFDA-JET Contributors* for the Pedestal and Edge Physics and the Steady State Operation Topical Groups of the ITPA

[1]MPI für Plasmaphysik, EURATOM Association, D-85748 Garching, Germany
[2]General Atomics, San Diego, California, USA
[3]Japan Atomic Energy Agency, 801-1 Mukouyama, Naka-shi, Ibaraki-ken, 311-0193, Japan
[4]EFDA Close Support Unit, D-85748 Garching, Germany
[5]UKAEA, EURATOM Association, Abingdon, UK
[6]CEA, EURATOM Association, Cadarache, France
[7]CIEMAT, EURATOM Association, Madrid, Spain
** See annex of M.L. Watkins et al, "Overview of JET Results ", (Proc. 21st IAEA Fusion Energy Conference, Chengdu, China (2006)).*

Preprint of Paper to be submitted for publication in
Nuclear Fusion

ABSTRACT.

Pedestal and global plasma parameters are compared in conventional ELMy H-modes and improved confinement discharges from ASDEX Upgrade (AUG), DIII-D, JET and JT-60U with varying net input power.Both electron and ion pedestal pressures are studied. The pedestal top pressure p^{PED} increases moderately with power in all tokamaks, in broad agreement with the power dependence of the IPB98(y,2) scaling. Higher pedestal pressures are observed in AUG improved H-modes and in JT-60U high β_{pol} discharges at $q_{95} \sim 6.5$ and high triangularity. For all machines and all scenarios a robust correlation between total and pedestal thermal stored energy is observed, with the ratio of the two varying between ~0.3 and 0.5. However the relative importance of pedestal and core confinement varies from regime to regime. In AUG the confinement improvement with respect to the IPB98(y,2) scaling is due to improved pedestal confinement in improved Hmodes with early heating and to both improved pedestal and core confinement in improved H-modes with late heating. In DIII-D hybrid discharges the increase in confinement factor compared to conventional H-modes is due to improved confinement in the plasma core. JT-60U reversed shear H-modes have strong internal transport barriers and thus improved core performance. In all four tokamaks improved edge stability is correlated to increasing total bpol and H98(y,2) increases with pedestal β_{pol}. The analysed multimachine data set supports a scaling expression for the pedestal stored energy derived under the assumption that the dominant loss term for the pedestal is by thermal conduction in the edge transport barrier region.

1. INTRODUCTION

The reference scenario for ITER is the standard H-mode with type I ELMs, a confinement factor H98(y,2) = 1 compared to the IPB98(y,2) confinement scaling [1] and a normalized beta value of $\beta_N = 1.8$. It is designed to reach a fusion gain Q = 10 with pulsed operation lasting for 400s. A second physics objective for ITER is to demonstrate Q = 5 operation in steady state plasma conditions. The performance of ITER could be significantly improved with a relatively small increase in energy confinement factor. Therefore, scenarios with H98(y,2) > 1 and high β_N would realise improved performance in ITER at the same plasma current (Q > 10) or could be used to achieve extended pulse duration at lower current, while maintaining $5 < Q < 10$. In the latter case one example is the hybrid scenario, which is designed to achieve long pulse operation with a combination of inductive and non-inductive currents.

Experiments in present day tokamaks show that one way to achieve this scenario is to modify the q profile of the discharge in such a way as to open access to operation at higher values of β_N. Generally, the addition of moderate heating during the plasma current ramp-up phase is considered the key to achieve a flat q-profile, with q ~ 1, due to slowing down of the current penetration into the plasma core. Subsequently, in the flat-top phase strong additional heating is applied to obtain the high β_N phase. The shape of the q-profile is thought to be an essential ingredient for the suppression of sawteeth, thereby eliminating seed-islands for the onset of detrimental Neoclassical

Tearing Modes (NTMs). However, small amplitude NTMs and sawteeth are often present in the high-β phase of the discharge, without severely affecting its performance.

In these discharges, due to the small power degradation of the energy confinement time with heating power, the H-mode confinement factor tends to be higher than in standard scaling laws, at least when compared to the widely used IPB98(y,2) scaling. On the other hand, the collisionality and beta dependence of this scaling expression are still under investigation [2]. In fact, there is a contradiction between the prediction of the IPB98(y,2) scaling expression, derived from a large multimachine database, which predicts a negative beta dependence of the global confinement time ($B\tau_{th}^{98(y,2)} \propto \beta^{-0.90}$), and the results of dedicated beta scans in DIII-D [3] and JET [4]. Conversely, dedicated beta scan experiments in JT-60U [5] and recently in ASDEX Upgrade (AUG) [6] show a clear negative beta dependence of the energy confinement time. Shaping effects as well as fuelling effects are possible causes of these differences [7], [6]. In parallel to these dedicated experiments, the ITPA group for confinement and database modelling is presently reworking the IPB98(y,2) confinement scaling law, with the inclusion of data sets of high beta discharges from AUG, DIII-D, JET and JT-60U. A general observation is that the change in confinement from the "conventional" or "standard" H-mode discharges to the improved confinement discharges is continuous and reflects the fact that these discharges occupy different areas (with some overlap) of the operating space of the ELMy H-mode.

One important question is how much of this improvement in confinement factor originates from the pedestal region, since the scaling of the H-mode pedestal is an open issue when predicting the performance of ITER. Initial studies on various machines have started to address this question [8], [9], [10], [11]. To continue this line of studies, this paper compares global and pedestal parameters in type I ELMy discharges with varying current profiles and input power from AUG, DIII-D, JET and JT-60U. In particular, the study is focussed on the variation of pedestal parameters as the input power is increased from conventional H-modes to improved confinement discharges. Candidates for improved confinement scenarios for ITER analysed in this paper include the improved H-mode in AUG [12, 13, 14], the hybrid discharges in DIII-D [15, 16], the hybrid discharges in JET [17] and the high-bpol [18] and the Reversed Shear (RS) ELMy H-modes [19] in JT-60U.

The paper is organized as follows: we first describe the set of discharges selected for this study (section 2) and the measurement and analysis techniques of the pedestal parameters (section 3). We then study the variation of the pedestal pressure as the input power is increased both in conventional H-modes and improved discharges (section 4). For AUG and DIII-D we can connect changes in the edge barrier pressure with changes of its gradient and width. In section 5 we study the relation between pedestal and global confinement and stability and compare our data base with a two-term model of the confinement in ELMy Hmodes. In section 6 we summarize the main results and draw the conclusions.

2. SELECTION OF THE MULTI MACHINE DATABASE

Conventional H-modes and improved confinement discharges were selected for each tokamak,

with the following general criteria: (i) ELMy H-modes with type I ELMs (and some mixed type I/ II at high triangularity, δ, for JET); (ii) discharges at safety factors $3 < q_{95} < 6$, for relevance to ITER; (iii) discharges with stationary phases at least 3 energy confinement times long. For each discharge the plasma parameters were averaged over the stationary phase. More specifically, the discharge selection was guided by the emphasis on the study of the variation of the pedestal with input power. The data sets chosen for each tokamak, however, reflect also the emphasis of the individual experimental programme, as well as the availability and range of edge diagnostics in the particular tokamak experiment. Although this data set serves as a good starting point for the studies reported here, the fact that it only includes data from existing scans means that the range of parameters covered is limited in some cases.

For continuity reasons, in this paper the labels “standard H-mode”, “hybrid discharge”, etc. used in the figures are those that had been assigned to the specific plasma discharge at the time it was run during a particular physics session. The analysis of this work shows that such “control room” definitions can lead to some ambiguity in the region of overlap of the operating spaces. A more physics based classification could be done in terms of Q scaling of the discharges compared to the ITER baseline and hybrid scenarios, but this goes outside the scope of this paper. We note, however, that work is ongoing at present in the fusion community to establish an agreed physics based definition for the improved confinement scenarios.

Table 1 summarizes the main plasma parameters of the discharges from the multimachine database assembled for the pedestal studies in this paper. Fig. 1 and 2 illustrate the data sets for each tokamak, in terms of H98(y,2) and density variation and total normalized beta and plasma inductance.

The AUG discharges were selected from the AUG pedestal database, namely the ELMy H-modes with the best pedestal measurements (see section 3) and therefore are not representative of the best performance discharges from AUG. From this database, standard and improved H-mode discharges were selected at $I_p = 0.8$ and 1.0MA, which are typical plasma currents for AUG, $3.65 < q_{95} < 5$ and $4.6 < n_e < 6.7 \times 10^{19} m^{-3}$, a density range common to both standard H-modes and improved H-modes contained in the pedestal database. In this data set the standard H-modes were run at different plasma shapes, whereas the improved H-mode discharges have all the same shape. The flat q-profile achieved in the improved H-mode is typically obtained by applying a combination of on- and off-axis Neutral Beam (NB) heating early in the discharge (improved H-mode with early heating, here labelled ‘IH early heating’). Experiments with delayed NB heating (here labelled as ‘IH late heating’), but maintaining the same combination of on- and off-axis NB heating, have produced discharges where the confinement is even better than in the early heating case [20, 21]. In these discharges the favourable q-profile with $q \sim 1$ is already established in the ohmic phase with current ramp up in the divertor configuration, before the additional heating is applied. With late heating (1,1) fishbones occur , rather than early (4,3) or (3,2) NTMs, which dominate the improved H-modes with early heating. This change in MHD behaviour is correlated with the higher confinement obtained with late heating [20] at intermediate input power levels. In the data set shown in Fig.2, in

terms of β_N there is a smooth transition from conventional to improved H-modes at β_N values ~ 2 - 2.5. The best performance improved Hmodes in this data set reach bN values ~ 3. Figures 1 and 2 show that based on a physics definition in AUG some of the discharges that have been labelled “standard H-modes” in the past are actually improved H-modes.

For DIII-D, standard H-modes and hybrid discharges at 1.2MA were selected. Operationally there is a separation in density between the hybrids and the conventional Hmodes, with the hybrid discharges run at low density. Nonetheless, a significant variation in confinement is found in the hybrid data at roughly constant density. Of the selected standard H-mode discharges, one set was run at the same plasma shape as the hybrid discharges ($\delta \sim 0.5$), and one at a different shape ($\delta \sim 0.3$). In the standard H-modes the additional heating is applied later in the discharge. In this data set the maximum input power reached in standard H-modes is 7.5MW and 10MW in the hybrid discharges.

For JET, standard H-mode discharges were selected from the studies reported in [10], which covered a variation in plasma current ($1 < Ip < 4$ MA), triangularity ($\delta = 0.23, 0.33, 0.43$) and safety factor ($2.7 < q_{95} < 4.6$) as well as density scans at various plasma currents. Of these data, only the discharges for which both ion and electron temperature profiles were available were retained for our study (see section 3). Therefore, all the high density discharges, for which the ECE diagnostic is in cut-off, are excluded, for instance all the discharges at 3MA. The conventional H-modes from JET analysed in this paper are thus at $I_p = 2.0$MA (low and high δ) and 2.5 MA (high δ). The JET hybrid discharges are a selection of the JET 2003/2004 hybrid experiments [17], again based on the availability of both T_i and T_e profiles. They include discharges at 1.4 and 2.0MA, with $3.8 < q_{95} < 4.1$, $\delta = 0.22, 0.45$ and are run at lower density than the conventional H-modes in our data set, $2 < n_e < 5\times10^{19}$ m^{-3}. The hybrid discharges are typically characterized by lower inductances, $li < 0.8$, and higher β_N, $2 < \beta_N < 2.8$, than the standard H-modes in this data set. The variation in net input power over the entire JET data set is $8 < P_{NET} < 22$MW. The β limit was not reached in these hybrid experiments.

For JT-60U, conventional type I ELMy H-modes were obtained in a series of H-mode experiments, such as triangularity effect on pedestal [22], toroidal field ripple effect on pedestal [23], and JET/ JT-60U similarity experiments [24]. Some of these discharges have weak internal transport barriers (ITBs) and are labelled as “high bpol H-mode” here. In contrast to these standard H-modes, “high bpol H-modes” and “RS H-modes” have ITBs, with positive and negative shear, respectively. Operationally, the high bpol H-mode is obtained by ramping up quickly the plasma current to avoid the appearance of sawteeth ($q(0) > 1$) and high power NB is injected into a low density ($n_e \sim 0.5$-1.0×10^{19} m^{-3}) target Ohmic plasma. In this paper, steady-state high β_{pol} H-modes [25] at $I_p = 0.9$MA ($q_{95} \sim 3.3$), quasi-steady high bpol H-modes [26] at $I_p = 1.0$MA ($6 < q_{95} < 6.6$) and 1.8MA ($3.2 < q_{95} < 4.2$) are selected, where the current profile was near its steady-state value. In the discharges at 1.8MA, full non-inductive current drive was obtained with bootstrap current and beam-driven current by the negative ion source based NBs. To obtain RS H-modes, low to medium

NB heating was applied during a quick Ip ramp to achieve the reversed shear current profile. Quasi-steady RS H-modes [19], [27] at $0.8 < I_p < 1.0$MA and $6.5 < q_{95} < 9$, with a large bootstrap current fraction are also included here. The maximum H98(y,2) value at 0.8MA is 2.4 (at $q_{95} \sim 9$) and full non-inductive current drive was obtained, with ~ 80% bootstrap current and 20% beam driven current. Although these discharges do not fully satisfy our selection criteria due to the high safety factor value, they are quite illustrative in contrasting the pedestal characteristics of the rest of the data base. We note here that most of the high bpol and RS H-modes of the JT-60U data set were not obtained in dedicated power scan experiments.

From the overview plots of Fig.1 and from table 1 we conclude that the main limitations of this data set are: (i) the poor overlap in plasma density between conventional Hmode and hybrid discharges in DIII-D and JET, (ii) the large variation in plasma shapes for AUG standard H-modes; (iii) the fact that the JET hybrid discharges did not reach the beta limit; (iv) the limited range in net input power for the JT-60U data and for the JET data at 2.5MA. Another possible drawback is that in the analysis of discharges from different experimental campaigns systematic uncertainties in the data can occur (e.g. due to diagnostic calibrations or conditions of the tokamak vessel).

This selected database for pedestal studies can be compared with the broader ELMy Hmode databases of Fig.3, which span the H-mode operating space of each device. The AUGdischarges are taken from the selection of ref. [21]. All discharges were run at plasma currents in the range I_p = 0.6–1.4MA and toroidal field B_t = 1.6 – 3.0T. The first data set includes all type I ELMy H-modes with $q_{95} < 5.5$ with stationary phases at least 0.2s long. The discharges marked as improved H-modes are the type I ELMy H-mode discharges with early heating plus some hand picked pulses with late heating, which reach stationary conditions for more than 0.5s and with $3 < q_{95} < 5$. The latter group does not contain only the best performance discharges realized at AUG. In fact, also the intermediate power phase (with moderate β_N and H factor) of discharges that at higher power achieve improved performance are included in this data set. The DIII-D standard H-modes data are obtained from version DB3v10 of the international global H-mode confinement database and were used in the development of the IPB98(y,2) scaling. In addition, the data shown in Fig.3 were selected so that the time rate of change of the stored energy was less than 10kW. The ELM phase for these data were labelled as either HSELM (H-mode Small ELM) or HGELM (H-mode Giant ELM). The discharges span a range of 0.3-2.0MA in plasma current, 0.9-2.1T in toroidal field and 0.8-15.5MW in thermal loss power. The hybrid discharges represent a range of operating conditions for hybrid discharges in DIII-D with $q_{95} \sim$ 4-5 and are taken from the data set used in Fig.1 of [14], which span a range of 1.1-1.3MA in plasma current, 1.7-1.9T in toroidal field and 4.4-11.1MW in thermal loss power. For JET, the ELMy H-mode data shown are from type I and mixed type I and II ELMy H-modes of the JET H-mode confinement database. The bulk of the discharges were run at $1.5 < I_p < 3$MA (although some discharges at I_p = 4MA are present), $2.7 < q_{95} < 3.5$ (but several discharges with q_{95} up to 5.5 are also included) and thermal loss power ranging from 5 to 20MW. The hybrid data are from the hybrid experiments carried out in 2003/2004, but without the restriction on the

availability of both Ti and Te measurements used for the plot of Fig.1. The JT-60U data are from a collection of data sets. The standard H-mode discharges were run at plasma currents $1.0 < I_p < 1.8$MA, safety factor $3 < q_{95} < 5.3$ and thermal loss power between 5 and 22MW. The high β_{pol} discharges where run at $0.9 < I_p < 1.8$MA, $3.2 < q_{95} < 6.5$ and thermal loss power in the range 6–22MW. The RS H-modes were run at plasma currents of 0.8–1.0 MA, with q_{95} in the range 6.5–9 and thermal loss power in the range 4 – 8MW.

In summary, the criteria used in the classification of the discharges of Fig.3 vary from one machine to the other and in all cases they are not based on a physics definition of the various regimes. This generates some confusion when comparing data from different machines. Some of the differences are actually apparent and would disappear if one were to choose a different (not necessarily physics based) but uniform selection criterion. For instance, the difference between AUG and DIII-D would reduce significantly if in the AUG plot only the improved H-modes at high beta were selected as improved H-modes and if, after reanalysis of all type I ELMy H-modes at high beta, those that achieved a flat q profile ~ 1 were re-labelled as 'improved H-modes'. Such a re-analysis of the AUG data base has not been possible so far. Comparison between the JET and AUG data sets of Fig.3 instead, shows a certain degree of similarity between the two machines. This is because the selection criteria for the "ELMy H-modes" data sets are roughly similar and the hybrid discharges included (from the 2003/2004 experimental campaigns) were run using the AUG improved H-mode recipe. We note also that, at the time, the JET hybrid scenario had not been fully developed. Recent experiments have extended the JET hybrid scenario and will be reported elsewhere. For JT-60U, the reversed shear H-modes show a large improvement in H98(y,2) confinement factor, however the IPB98(y,2) scaling was not developed including discharges with strong internal transport barriers at large safety factors.

For the purpose of the studies reported in this paper, however, we conclude that the selected data base for pedestal studies illustrated in Fig. 1 and Table 1 gives a fair representation of the operating ranges of the scenarios from the four tokamaks compared in this study.

3. PEDESTAL MEASUREMENTS AND ANALYSIS TECHNIQUES

The pedestal top pressure, p^{PED}, is the most accessible parameter in the Edge Transport Barrier region (ETB) and can be supplied by all four tokamaks. However there are sufficient differences in the measurement of the pedestal parameters and in the techniques utilized for the analysis of the pedestal profiles that it is worth giving here a brief description of the methods used for the derivation of the data contained in this study.

An additional aim of this paper is to include both electron and ion pedestal pressures in the analysis, $p_e^{PED} = n_e^{PED} \times T_e^{PED} \times e$ and $p_I^{PED} = n_I^{PED} \times T_i^{PED} \times e$, where n_I is the sum of the deuteron and impurity ions density and T_i is the ion (generally C+6) temperature, assumed to be equal to the plasma background ion temperature and to the temperature of any other low-Z impurity ions that may be present in the plasma. Thus the total pedestal top pressure is calculated directly as

the sum of the two: $p^{PED} = p_e^{PED} + p_I^{PED}$. Although this criterion i restrictive in the selection of discharges that can be analysed, it is supported by the finding described in section 4, that the variation of the electron and ion pedestal pressures is systematically different as the input power is increased.

For AUG, edge Te profiles were obtained combining high resolution measurements from the Thomson Scattering (TS) system [28], [29] and the 60-channel ECE heterodyne diagnostic. The edge electron density profiles were obtained combining high resolution measurements from the TS system, the edge Li-beam diagnostic [30] and the line averaged density of the FIR interferometer. A composite profile was generated from all profiles collected within the selected stationary time window and then fit by a modified hyperbolic tangent function [31], [32], which joins a polynomial function in the core and one in the scrape-off-layer. At present, high resolution measurements of the ion edge transport barrier (ETB) are not possible on a routine basis in AUG. For the AUG discharges analysed in this paper, the pedestal top ion temperature, T_i^{PED}, was thus obtained by fitting the Ti profile measured by core CXRS with 30 to 50 ms time resolution, imposing a fixed pedestal width (2cm, i.e. of the order of the electron temperature widths measured in AUG, see section 4.2) and radial position for the ion ETB, using a similar fitting function as that for the edge electron profiles. This carries some uncertainty in the determination of T_i^{PED} and, therefore, of p_i^{PED}. The T_i profiles are obtained from the C VI charge exchange line emission at 5290.5Å (n = 8 - 7 transition).

For the evaluation of the contribution of the pedestal to the global confinement the pedestal top parameters are deduced from the profile fits to data from all phases of the ELM cycle (ELM-averaged technique). The correct procedure, however, would be to fit the pedestal pressure across each ELM cycle and then perform the time average over the selected stationary time window. This procedure is too demanding when analysing a large number of discharges. For one AUG case we have fitted separately the edge profiles at regular time intervals during one ELM cycle and then taken the time average of the pedestal top values. The two analysis techniques yielded very similar pedestal top values for this test case, as shown in Fig.4. This test gives us confidence that the ELM averaged technique is appropriate for the evaluation of the pedestal stored energy, W_{PED}.

For DIII-D, the electron temperature and density profiles were measured by a multiplepoint TS system [33]. The electron density from this system was adjusted to match the lineaveraged density from a CO_2 interferometer. The adjustments were typically of order 10-15%. Composite profiles for T_e and ne were then obtained in the time window of interest. Laser pulses which were close to ELMs were removed by an ELM detection scheme based on the use of D-alpha signals. The data for each profile were mapped to normalized y with a magnetic equilibrium generated at the time when the data were acquired. For both Te and ne the experimental data and the flux coordinates within a time window were then grouped and fit in the same way as described above for the AUG profiles. After this fit, both T_e and ne profiles were shifted in y space by an amount required to align the foot of the tanh function for the T_e profile with the plasma separatrix. A consistency check of the fits was performed, showing that the pedestal top electron pressure p_e^{PED} values obtained from the fit of the pressure profiles are essentially the same as p_e^{PED} obtained by multiplying n_e^{PED} and

T_e^{PED} obtained from the respective fits, as shown in Fig.5. The ion temperature and carbon density were obtained from the C VI charge exchange line emission at 5290.5 ≈ from CXRS [34]. As with the TS data, the CXRS data were taken from multiple frames obtained during each time window, but no spatial adjustment was performed on these data. The Ti profiles were fit in a similar way as the one described for the electron profiles.

In JET the electron temperature pedestal top value is determined at the radial position where the T_e profile measured by the ECE radiometer [35] changes slope, typically in the region of $\rho_{pol} \sim 0.9$. Lacking profile information, the electron density pedestal top (n_e^{PED}) is assumed to be equal to the line averaged density measured by the edge channel of the FIR interferometer. This assumption can overestimate of the pedestal top density in the case of peaked density profiles, typically at low density. T_i^{PED} is obtained from the edge T_i profile, measured by the edge CXRS diagnostic [36] from the C VI charge exchange line emission at 5290.5Å. Since the spatial resolution of the edge CXRS system does not allow for unambiguous determination of T_i^{PED}, this was assumed to be equal to the value of the T_i profile at the same radial position as T_e^{PED}. This can lead to an uncertainty of at least 20% in the value of T_i^{PED}. The pedestal top values are the average of the corresponding quantities over the chosen stationary time window.

In JT-60U the electron temperature and density profiles were obtained from TS measurements [37, 38]. The absolute value of the electron density was normalized to match the line averaged density from vertical and/or horizontal interferometers. Electron profiles for the experiments in [24] and [25] were taken at one time slice between (or just before) ELMs, and those for the other experiments were averaged over several laser pulses. The ion temperature profiles were measured by a combination of core and edge CXRS [39] with a time resolution of 50Hz and are ELM-averaged. The pedestal top electron temperature and density and ion temperature were obtained by bilinear fits of the respective profiles.

For DIII-D n_I^{PED} is calculated from ΔZ_{eff} from CXRS and for JET and JT-60U n_I^{PED} is calculated from Z_{eff} measured by visible bremsstrahlung, assuming that carbon is the dominant impurity. In AUG the carbon concentration has been observed to decrease with increasing tungsten coverage of the vessel walls [40]. For the standard H-modes analysed in this paper we have assumed an average carbon concentration of 1.5% and an average helium concentration of 10% (due to frequent glow discharge cleaning in between plasma discharges). For the improved H-mode discharges the impurity densities of the main intrinsic impurities have been measured by CXRS, with $n_I^{PED} = (n_D/n_e + n_{He}/n_e + n_B/n_e + n_C/n_e) \times n_e^{PED}$, where n_B/n_e is the boron concentration, significant for the discharges run after a fresh boronization of the vessel. For JET, Zeff measured by visible bremsstrahlung with a vertical line-of-sight through the plasma core is compared with ΔZ_{eff} due to carbon obtained by core CXRS. The two measurements are generally found to be inconsistent, with the bremsstrahlung measurement yielding a higher Z_{eff}. In our data set the ratio of the two Z_{eff} values can be as high as a factor of two. The reason for this discrepancy is not yet understood. For consistency with the parameter selection in the JET ELMy H-mode database we have chosen to use Z_{eff} from visible

bremsstrahlung in our analysis, bearing in mind that we are thus likely tooverestimate Z_{eff} in the JET data set. In the worst case this would correspond to an underestimation of the pedestal ion pressure of order 20%.

4. POWER DEPENDENCE OF PEDESTAL PARAMETERS

4.1. POWER DEPENDENCE OF PEDESTAL TOP PRESSURE

In conventional type I ELMy H-modes the total thermal stored energy is correlated to the pedestal stored energy. For the scenarios considered in this study, all machines show a robust correlation between pedestal stored energy W_{PED} and total thermal stored energy, W_{th}. We define here the total thermal stored energy $W_{th} = W_{core} + W_{PED}$, with W_{core} the core thermal energy content and $W_{PED} = 3/2\ p_{PED} \times Vol$, where Vol is the total plasma volume. In particular, in all four tokamaks higher global stored energies are correlated with higher pedestal energies and the ratio W_{PED}/W_{th} is similar, ranging from about 0.30 to 0.50. Furthermore, the ratio W_{PED}/W_{th} is in the same range for conventional H-modes and improved confinement scenarios as shown in Fig.6. The only exception in this trend are the RS H-modes from JT-60U, for which Wth increases due to increasing core stored energy.

A more subtle issue is to what extent the improved performance of these scenarios is due to differences in the Edge Transport Barrier (ETB) region compared to conventional Hmodes. In terms of global plasma parameters, this issue can best be studied in power scans at otherwise fixed plasma parameters, since the pedestal plasma pressure varies by changing plasma current, input power, density, plasma shape or isotope composition of the plasma, see e.g.[41]. As we have pointed out in section 2, such power scans are not available in all four tokamaks (and both for conventional and improved scenarios). At present, they are being proposed for future experiments. For this reason, in this section we compare the dependence of the pedestal pressure on input power for conventional H-modes and improved scenarios by grouping the discharges by plasma current, shape and operating mode.

Figure 7 shows the variation of p^{PED} with P_{NET} in the 4 tokamaks. In order to guide the eye, curves of $p^{PED} \sim P_{NET}^{0.31}$ have been added for each plasma current. These curves represent the power scaling of the IPB98(y,2) H-mode confinement scaling at a given current. We observe a general trend in all tokamaks for p^{PED} to increase with input power along this curve for most of the discharges at a given plasma current. Compared to this trend, higher pedestal pressures are found in AUG in improved H-modes with late heating and with early heating at high input power and in JT-60U for the high bpol discharges at $q_{95} = 6.5$ and high triangularity.

In addition to this general trend, characteristics specific to each machine are also observed. In AUG standard H-modes at 0.8MA there is a significant variation in p^{PED} with P^{NET}, due to variations in plasma shape. Part of the scatter may also be due to the uncertainties in p_i^{PED}, as discussed in section 3. At 1.0MA, due to the absence of power scans in standard H-modes at relatively constant density, it is hard to draw a comparison with improved Hmodes at the same current. Also, the plasma shape was not the same in the two cases.

In DIII-D p^{PED} increases with PNET following the IPB98(y,2) scaling both in the standard H-modes and in the hybrid discharges analysed. For the standard H-modes at low triangularity part of the increase in p^{PED} with power is due to an increase with density, since density and power variation are coupled for this group of discharges.

In JET, also due to uncertainties in p_i^{PED} there is a comparatively large scatter in the total pedestal pressure, so that it is not possible to separate the increase of p^{PED} with current from that with PNET at 1.4 and 2.0MA in this data set. The pedestal top pressure increases with power roughly in the same way in the standard H-modes and in the hybrid discharges. In the hybrid discharges the input power is correlated to the plasma triangularity. The conventional H-modes at 2.5MA do not cover a sufficiently broad power range in order to determine trends, but are plotted for comparison.

In JT-60U, the pedestal top pressure in RS H-modes ($0.8 < I_p < 1.0$MA) varies with input power in a similar way as the standard H-modes and high β_{pol} discharges at low q_{95} at 1MA. In the high β_{pol} discharges at high q_{95} and high triangularity p^{PED} is higher than the scaling predicts at this plasma current. However, due to the limited number of data points, it is not possible to conclude if the higher pedestal pressure is due to a weaker power degradation than predicted by the IPB98(y,2) scaling or to the effect of high triangularity. Interestingly, these discharges are characterized by the presence of ITBs and the plasma internal inductance is li ~0.7, lower than for the rest of the high β_{pol} dataset. At 1.8MA there isn't enough variation in input power to draw any firm conclusion from the data.

In summary, analysis of the variation of the pedestal top pressure with input power in our data set shows that the IPB98(y,2) scaling law describes fairly well the moderate increase of pedestal pressure with power, $p^{PED} \sim P_{NET}^{0.3}$1. However, there are two notable deviations from the scaling in our data set, namely the AUG improved H-modes with late heating and with early heating at high power at 1.0MA and the JT-60U high β_{pol} discharges at $q_{95} \sim 6$ and high triangularity. In these regimes this deviation points to an improvement in confinement factor due to improved pedestal confinement.

4.2. POWER DEPENDENCE OF THE EDGE TRANSPORT BARRIER WIDTHS

The measurement of the edge transport barrier widths requires very high spatial resolution at the plasma edge, which is only possible in AUG (for T_e and n_e) and in DIII-D (for T_e, n_e and T_i). In this section we compare measurements of the pedestal widths from the AUG and DIII-D discharges as the input power is increased. For both machines the pedestal width data are mapped to the outer midplane.

In order to reduce the scatter due to ELMs in the measurement of the widths and gradients of the ETB region, in AUG an ELM-synchronized analysis of the edge profiles is performed [32]. In the stationary time window of interest, the edge profiles are selected over short time windows (typically 2-3ms) during the ELM rise period, equidistant from each ELM and then fitted using the method described in section 3. Using this technique, it is found that as the net input power is increased in

the improved H-modes power scan the width of the density ETB (Δn_e) stays roughly constant, whereas the T_e ETB (ΔT_e) broadens with power. The pedestal top density tends to increase with power (in the absence of gas fuelling) due to a combination of steepening of the density gradient in the ETB and of increasing density in the scrape-off-layer, which raises the base level of the density barrier [42]. The pedestal top temperature also increases with power, due to an increase of the width of the temperature ETB. At high power îne is narrower than ΔT_e, with $\Delta n_e \sim 1$cm and $2 < \Delta T_e < 3$cm, as shown in Fig.8, in contrast to previous analysis on lower power conventional H-modes [32]. In improved H-modes with late heating, Δn_e and ΔT_e are similar to those measured with early heating, both in absolute magnitude and in variation with input power.

The variation of the ETB widths with input power for the DIII-D discharges is shown in figure 9. In DIII-D, the density ETB is broader and the density gradient is less steep for hybrid discharges than for standard H-mode discharges. Since both the input power and the density are systematically different in these data sets, it is not possible to conclude whether this is a power or a density effect (or a combination of the two). The electron and ion temperature ETBs broaden with input power in a continuous way from conventional H-modes to hybrid discharges. The widths of the n_e and T_e ETBs are of comparable magnitude, with $1 < \Delta n_e \sim \Delta T_e < 3$cm, while the ion temperature pedestal is much broader at high power, with an overall variation of $2 < \Delta T_i < 7$cm. At high power, a steepening of the T_i gradient in the ETB is also observed. Therefore, the increase of piPED at high power is due to an increase of both width and gradient of the ion temperature pedestal. The increase in p_e^{PED} at high power, instead, is due solely to an increase in width of the T_e ETB. Based on these results, we could speculate that at high power the total pedestal pressure in AUG and JET might be underestimated in our study due to the assumption of $\Delta T_e = \Delta T_i$ made in the previous section.

5. RELATION BETWEEN PEDESTAL AND GLOBAL CONFINEMENT AND STABILITY

In order to study the relation between pedestal and global confinement as the input power is increased, we first consider the variation of the pedestal and core thermal stored energy, W_{PED} and $W_{core} = W_{th} - W_{PED}$. Subsequently we compare the results from the four machines in terms of normalized pressure.

Figure 10 shows that at a given plasma current there is a general trend for W_{th} to increase with input power roughly as $P_{NET}^{0.31}$ in all tokamaks, that is, in line with the power scaling of the IPB98(y,2) scaling expression. Higher stored energies, compared to this trend, are found in AUG for the improved H-modes with late heating and for the improved H-modes with early heating at the highest power, in DIII-D for the hybrid discharges at high power and in JT-60U for the high bpol discharges at $q_{95} = 6.5$ and for the RS H-modes (where higher global stored energies are achieved at lower heating power). In JET no significant difference between standard H-modes and hybrid discharges is observed in terms of power variation of W_{th}.

Since according to our definition the total stored energy is the sum of the energy content in the

core and in the pedestal, the correlation between W_{th} and W_{PED}, as shown in Fig.6, intrinsically contains a co-linearity between the two quantities, which doesn't easily reveal whether the increase in total stored energy with power is primarily driven by the core or by the pedestal. For this reason, we plot in Fig.11 the relation between core and pedestal stored energy for the four tokamaks. From Fig.7 and 10 we have seen that as the net input power is increased, certain scenarios perform "better" with respect to the IPB98(y,2) power scaling (or, alternatively, that the power degradation is weaker in these regimes). In particular, the AUG improved H-modes at 1.0MA with late heating and with early heating at high power exhibit pedestal and total stored energies above the $P_{NET}^{0.31}$ curve, whereas the DIII-D hybrid discharges exhibit total stored energies above the IPB98(y,2) power scaling, while the pedestal energy follows the scaling. In JT-60U RS H-modes the pedestal stored energy follows the IPB98(y,2) power scaling, as in the case of the bulk of the standard and high β_{pol} H-modes, while W_{th} does not. Fig.11 indicates that in the DIII-D hybrid discharges of the present data set the improvement in confinement factor at high power is primarily due to improved core confinement compared to conventional H-modes. We note, however, that due to the scatter in the data a linear relation between W_{core} and W_{PED} cannot be completely excluded, which would simply that the confinement improvement is due to better confinement in the pedestal, for stiff profiles. Analysis of a broader data set compared to the present one, as well as new dedicated power scans in standard H-modes and hybrid discharges are needed to clarify this issue. In JT- 60U RS H-modes Wcore increases significantly at fixed W_{PED}, showing decoupling of W^{core} from W_{PED} in the presence of strong ITBs. In contrast, both in standard H-modes and in high β_{pol} H-modes there is a linear correlation between pedestal and core stored energy. In the JET hybrid discharges at 1.4MA, W_{th} increases with power and triangularity due to an increase of W_{PED} while W_{core} remains unvaried. For the remaining JET data set the overall correlation between W_{core} and W_{PED} is clearly driven by the increase in plasma current. In AUG the improvement in confinement factor obtained at high input power in improved H-modes with early heating is due primarily to higher pedestal stored energies compared to the IPB98(y,2) scaling. In the improved H-modes with late heating an improvement in core confinement is also observed, leading to the higher total stored energy observed in these discharges [20].

In figures 12, 13 and 14 the multimachine database is analysed in terms of normalized parameters. Fig.12 shows that the pedestal normalized beta, $\beta_{N,PED}$, is correlated to the total thermal beta, $\beta_{N,th}$, in all 4 tokamaks. In addition, all machines display similar ranges in thermal beta, although for JT-60U they are obtained through a stronger contribution of the core pressure.

For JT-60U it has been shown [43] that in type I ELMy discharges the pedestal β_{pol} is a measure for edge stability and that both energy confinement factor and total normalized pressure increase with improved edge stability for type I ELMy H-modes with and without ITBs [11]. This relation is valid especially at high triangularity and in the plasma current range I_p = 0.8–1.8MA. Similar studies have also been reported for DIII-D [9]. Figure 13 shows that for all four tokamaks the pedestal bpol increases roughly linearly with the total bpol. This correlation indicates either that

improved edge stability is due to increased Shafranov shift or that increased pedestal stored energy leads to increased total stored energy through temperature profile stiffness, in the absence of ITBs. It is however not possible to determine at this stage whether an increase in total β_{pol} drives an improvement in edge stability or vice versa or if both mechanisms are at play in a continuous loop. While AUG, DIII-D and JET are aligned along a similar slope, for JT-60U most of the increase in total bpol is sustained by core pressure, except for the high bpol discharges at high q_{95}. Figure 14 shows that there is also a general trend for H98(y,2) to increase with pedestal β_{pol} for the analysed discharges. However, in each tokamak a variation in H98(y,2) at constant pedestal β_{pol} is observed, which is linked with core confinement improvement in AUG, DIII-D and JT-60U RS H-modes. The high β_{pol} discharges in at $q_{95} \sim 6$ in JT-60U have a moderate H-factor at higher values of pedestal β_{pol}.For JT-60U the weaker role of the edge stability is compensated by the core in the energy confinement factor, since there is no clear separation amongst the four tokamaks in terms of H98(y,2) versus pedestal bpol.

Finally, we compare the database with the two-term model for pedestal and core confinement of Cordey et al. [44]. In that work, two physical models for the pedestal are calibrated against the joint pedestal and core database. In the first limiting model, the thermal conduction model, it is assumed that the dominant loss term for the pedestal is by thermal conduction down the steep gradient region of the edge transport barrier. We compare our data with the modified scaling expression of eq. (2) in [44], which restricts the data set to type I ELMy discharges only, since this corresponds to the selection of the data set for our work:

$$W_{PED,fit} = 0.00807\ I_p^{1.41}\ R^{1.37}\ P^{0.50}\ n_e^{-0.15}\ B_t^{0.32}\ m^{0.2}\ F_q^{1.61}\ k_a^{1.21}$$

where I_p is the plasma current [MA], R the major radius [R], P the thermal loss power [MW], n_e the density ($10^{19}\ m^{-3}$), Bt the toroidal field [T], m the atomic mass, ka the elongation (= Vol/(2 πR)/(π a2)), Fq = q_{95}/q_{cyl}, and $q_{cyl} = 5\ k_a\ a^2\ B_t/R\ I_p$, as defined in [44]. The comparison between this scaling expression, WPED,fit, and the pedestal stored energies of this work is shown in Fig.15. For consistency, we have also multiplied the pedestal stored energy by the factor Cv = 0.92, representing the fraction of the total volume occupied by the pedestal [45] as in ref [44]. The core stored energy data are compared with $W_{core,fit1}$ of eq. (7) of [44]:

$$W_{core,fit1} = 0.103\ I_p^{0.88}\ R^{2.02}\ P^{0.25}\ n_e^{0.49}\ B_t^{0.11}\ k_a^{0.24}\ \varepsilon^{1.22}\ m^{0.23}$$

where ε is the inverse aspect ratio.

In the second limiting model, the MHD limit model, it is assumed that ELMs losses are dominant for the pedestal and that the pressure gradient in the pedestal is determined by an MHD stability limit due to ballooning or peeling modes. In this case we compare our data with the expression for $\beta_{ped} = W_{PED}/R\ I_p^2$ of eq. (5) and $W_{core,fit2}$ of eq. (8) of ref. [44]:

$$\beta_{ped} = 6.43 \times 10^{-4}\, \rho^{*0.3}\, m^{0.2}\, F_q^{\,2.18}\, \varepsilon^{-2.67}\, k_a^{\,2.27}$$

$$W_{core,fit2} = 0.151\, I_p^{\,0.68}\, R^{2.32}\, P^{0.42}\, n^{0.59}\, B^{0.13}\, k_a^{\,-0.34}\, \varepsilon^{1.96}\, m^{0.34}$$

where $\rho^*_{ped} = T_{pav}^{\,1/2}/I_p$, $T_{pav} = 2 \times 10^2\, W_{PED}/C_v\, Vol\, n_{PED}$, and T_{pav} and n^{PED} are the average pedestal temperature and density, as defined in [44]. We use here $n^{PED} = n_e^{PED} + n_I^{PED}$. The comparison of our data set with the scaling expressions for the MHD limit model is shown in Fig. 16.

The experimental stored energies of our data set are in broad agreement with the scaling expression for the thermal conduction model. Moreover, both standard H-modes and improved confinement discharges follow the same scaling. However, the DIII-D discharges, some of the AUG improved H-modes and the JET hybrid discharges at 1.4MA display higher pedestal stored energies than predicted by the model. This could be due to the fact that in our data set the ion pressure is often larger than the electron pressure, while in the data base used for the calibration of the two-point model $p_e = p_i$ was assumed for most discharges. A large scatter is found in the pedestal stored energy for the standard H-mode discharges of AUG. As already discussed in section 4, this is due to the broad range of plasma shapes of these discharges. Although the scaling $W_{PED,fit}$ includes some shaping factors through the variables F_q and k_a, more subtle parameters such as triangularity and squareness are not included in the model. These parameters are known to influence the edge stability and the pedestal height and can lead to variations of the pedestal pressure of up to a factor of 2 [46]. In ref. [10] comparison of JET standard H-mode data with the two-point model could not discriminate between the two physics models for the pedestal. On the contrary, the multimachine pedestal data analysed in this paper are in clear disagreement with the MHD limiting model for the pedestal. It is interesting to note that in our case we find broad agreement with the scaling expression which explicitly contains a power dependence of the pedestal stored energy. The power dependence in the thermal conduction limiting model, $W_{PED} \propto P^{0.5}$, rather than $W_{PED} \propto P^{0.31}$ as in the one-term IPB98(y,2) scaling, may be more appropriate in describing our data set. However, on average a higher degree of accuracy is still needed in the measurement of the pedestal pressure in order to distinguish between these two moderate power dependencies.

The core stored energy data of our database are in broad agreement with the fits for both models. This is interesting because compared to the core database used in the work of Cordey et al., which only contained discharges with no MHD activity in the core, at least the hybrid discharges from AUG, DIII-D and JET analysed in this paper display core MHD activity (typically benign (3,2) and (4,3) NTM's, fishbones) which can lead to some deterioration of the core energy confinement. However, typically these discharges are also characterized by higher plasma rotation and larger T_i/T_e ratios as compared to the conventional H-modes, properties correlated with improved confinement. Not surprisingly, the largest deviation from both models are found for the RS H-modes from JT-60U, since in the work of ref. [44] discharges with reversed shear were not included.

CONCLUSIONS

In this paper we have compared pedestal and global parameters in conventional ELMy H-modes and improved confinement discharges realised with varying input power and current profiles in AUG, DIII-D, JET and JT-60U. In particular, both electron and ion pedestal pressures have been studied. The transition from "standard H-modes" to improved confinement scenarios is continuous with increasing input power, with overlap in the operating space. Based on physics analysis rather than "control room labels" some of the discharges analysed in the paper would be labelled differently.

The variation of the pedestal parameters as the input power is increased from standard H-modes to improved confinement scenarios is continuous and does not lead to a bifurcation. In all four tokamaks, a general trend is observed for the pedestal top pressure to increase moderately with net input power, roughly in agreement with the power dependence of the IPB98(y,2) scaling expression, $p_{PED} \propto P_{NET}^{0.31}$. Compared to this general trend, at the highest input powers higher pedestal pressures are found in AUG improved H-modes and in JT-60U high β_{pol} discharges at $q_{95} = 6.5$ and high triangularity.

Analysis of the pedestal structure shows that in AUG improved H-modes p^{PED} increases with power due to an increase of both n_e^{PED} (steepening of the density gradient in the ETB and of increasing density in the SOL, which raises the base level of the density barrier) and TePED (increase of the width of the temperature ETB). In DIII-D p^{PED} increases primarily due to an increase of the pedestal temperature via an increase in width of the T_e ETB and an increase of both width and gradient of the T_i ETB. This result highlights the importance of the study of both electron and ion pedestal pressures, since they have a systematic variation with power.

For the scenarios considered in this paper, all machines show a robust correlation between total thermal stored energy W_{th} and pedestal stored energy W_{PED}. In addition, the ratio W_{PED}/W_{th} is similar in all machines, varying from about 0.3 to 0.5 and is in the same range both for conventional H-modes and improved confinement scenarios. However, the relative importance of edge and core confinement varies from regime to regime, often even in the same machine. For AUG improved H-modes, the improvement in confinement factor obtained at high input power is due to increased pedestal stored energy compared to conventional Hmodes at lower power. In addition, in the improved H-modes with late heating an improvement in core confinement is also observed. In the DIII-D hybrid discharges the improved confinement appears to be primarily due to improved confinement in the plasma core as compared to conventional H-modes. In the JT-60U data set, conventional and high β_{pol} H-modes have similar values of pedestal and core stored energy. Note, however, that high β_{pol} H-modes at high triangularity can achieve simultaneously high values of pedestal and core β_{pol} [11], while maintaining the correlation between the two. Reversed shear H-modes, instead, have strong internal transport barriers and thus improved core performance, independent of the pedestal energy content. In the JET hybrid discharges analysed no significant improvement in confinement factor is observed compared to conventional H-modes.

In all four tokamaks a roughly linear correlation between pedestal β_{pol} and total β_{pol} is found,

indicating a close correlation between edge and global stability. However it is not possible to distinguish if an improvement in edge stability leads to higher total beta or if an increase in Shafranov shift is a cause for improved edge stability. It is also possible that both mechanisms are at play simultaneously, reacting to each other in a continuous loop. A general trend for H98(y,2) to increase with pedestal β_{pol} is also observed, although with variations in H98(y,2) at constant pedestal β_{pol} in each machine.

The multimachine pedestal data analysed in this paper support the scaling expression of WPED derived in ref. [44] under the assumption of the thermal conduction limiting model, as opposed to the MHD limiting model for pedestal energy losses.

ACKNOWLEDGEMENTS:

We are grateful to J. De Boo, D.C. McDonald and the ITPA group of confinement and data base modelling for providing the hybrid data for DIII-D and JET contained in Fig.3. Work supported in part by the US Department of Energy under DE-FC02-04ER54698

REFERENCES:

[1]. ITER Physics Basis, Nucl. Fusion **39** (1999) 2137.
[2]. McDonald, D.C. et al., Proc. 21st FEC 2006, Chengdu, China, EX/P3-5.
[3]. Petty, C.C., et al., Physics of Plasmas **11** (2004) 5.
[4]. McDonald, D.C., et al., Plasma Phys. Control. Fusion **46** (2004) A215.
[5]. Urano, H., et al., Nucl. Fusion **46** (2006) 781.
[6]. Vermare, L., et al., "Study of the beta dependence of confinement and heat transport in ASDEX Upgrade", submitted to Nucl. Fusion.
[7]. Takizuka, T., et al., Nucl. Fusion 48 (2006) 799.
[8]. Maggi, C.F., et al., Proc. 32nd EPS Conf., Tarragona, Spain, 2005.
[9]. Groebner, R.J., et al., Plasma Phys. Control. Fusion **48** (2006) A109.
[10]. Sartori, R., et al., Proc. 20th FEC 2004, Vilamoura, Portugal, EX/6-3.
[11]. Kamada, Y., et al., Plasma Phys. Control. Fusion **48** (2006) A419.
[12]. Gruber, O., et al., Phys Rev. Lett. **83** (1999) 1787.
[13]. Sips, A.C.C., et al., Plasma Phys. Control. Fusion **44** (2002) A151.
[14]. Peeters, A., et al., Nucl. Fusion **42** (2002) 1376.
[15]. Wade, M.R., et al., Nucl. Fusion **45** (2005) 407.
[16]. Luce, T.C., et al., Phys. Plasmas **11** (2004) 2627.
[17]. Joffrin, E., et al., Nucl. Fusion **45** (2005) 626.
[18]. Kamada, Y. and JT-60U TEAM, Nucl. Fusion **41** (2001) 1311.
[19]. Fujita, T., et al., Phys. Rev. Lett. **87** (2001) 085001.
[20]. Stober, J.K. et al., "Physics studies of the improved H-mode scenario in ASDEX Upgrade", to be submitted to Nucl. Fusion.

[21]. Sips, A.C.C. et al., Proc. 21st FEC 2006, Chengdu, China, EX/1-1.
[22]. Urano, H., et a l., Plasma Phys. Control. Fusion **44** (2002) 11.
[23]. Urano, H., et al., Plasma Phys. Control. Fusion **46** (2006) A193.
[24]. Saibene, G., et al., Proc. 20th FEC 2004, Vilamoura, Portugal, IT/1-2.
[25]. Oyama, N., et al., Proc. 21st FEC 2006, Chengdu, China, EX/1-3.
[26]. Kamada, Y., et al., Plasma Phys. Control. Fusion **44** (2002) A279.
[27]. Fujita, T., et al., Nucl. Fusion **42** (2002) 180.
[28]. Murmann, H, et al., RSI **63** (1992) 4941.
[29]. Kurzan, B, et al., Plasma Phys. Control. Fusion **46** (2004) 299.
[30]. Fiedler S., et al, J.Nucl.Mat. **266-269** (1999) 1279.
[31]. Groebner, R.G., et al., Phys. Plasmas **5** (1998) 1800.
[32]. Horton, L.D., et al., Nucl. Fusion **45** (2005) 856.
[33]. Carlstrom, T.N., et al., RSI **63** (1992) 4901.
[34]. Gohil, P., et al., in Proc. 14th Symp. In Fusion Engineering, San Diego, 1991, Vol. 2, Inst. of Electrical and Electronics Engineers, New York (1992) 1199.
[35]. De La Luna, E., et al., RSI **75** (2004) 3831.
[36]. Hawkes N. and Peacock N., RSI 63 (1992) 5164.
[37]. Yoshida, H., et al., RSI **70** (1999) 751.
[38]. Hatae, T., et al., RSI **70** (1999) 772.
[39]. Koide, Y., et al., RSI **72** (2001) 119.
[40]. Kallenbach, A., et al., PSI Conf. 2006, JNM in press.
[41]. Saibene, G., et al., Nucl. Fusion **39** (1999) 1133.
[42]. Horton, L.D., et al., Proc. 33rd EPS Conf. 2006, Rome, Italy.
[43]. Kamada, Y., et al., Plasma Phys. Control. Fusion **44** (2002) A279.
[44]. Cordey, J.G., et al., Nucl. Fusion **43** (2003) 670.
[45]. Thomsen, K., et al., Plasma Phys. Control. Fusion **44** (2002) A429.
[46]. Leonard, A.W., et al., Proc. 21st FEC 2006, Chengdu, China, EX/P8-3.

Tokamak	Scenario	I_p (MA)	n_e (10^{19} m^{-3})	q_{95}	δ	P_{NET} (MW)
AUG	Standard	0.8	5.0 – 6.7	3.7 – 5.1	0.14 – 0.44	4.0 – 8.0
	H-modes	1.0	4.7 – 6.7	3.2 – 4.4	0.13 – 0.34	4.4 – 5.8
	Improved	0.8	5.3 – 5.9	4.8	0.22 – 0.26	5.0 – 11.1
	H-modes	1.0	4.9 – 6.0	4.6		7.5 – 11.8
DIII-D	Standard	1.2	6.4 – 10.0	4.3	0.3	3.5 – 7.2
	H-modes		6.0	4.2	0.5	3.6 – 6.7
	Hybrid Discharges	1.2	5.0	4.2 – 4.5	0.5	4.5 – 9.2
JET	Standard	2.0	4.8 – 5.6	3.6 – 3.8	0.25 – 0.43	10.3 – 17.8
	H-modes	2.5	6.3 – 8.0	3.0 – 4.6	0.43	14.4 – 17.5
	Hybrid	1.4	2.1 – 3.8	3.5 – 4.1	0.22, 0.45	8.7 – 17.6
	Discharges	2.0	3.1 – 5.6	3.8 – 4.0	0.21, 0.42	15.8 – 21.2
JT-60U	Standard	1.0	1.5 – 3.8	3.0 – 5.3	0.13 – 0.49	5.1 – 10.9
	H-modes	1.8	3.4 – 4.0	3.1	0.26	10.7 – 14.2
	High β_{pol}	0.9, 1.0	2.0 – 3.5	3.3–5.2; 6.5	0.27; 0.47	6.6 – 20.7
	H-modes	1.8	3.3 – 4.0	3.1; 4.0	0.27; 0.34	13.0; 22.0
	RS H-modes	0.8 – 1.0	1.8 – 2.8	6.5 – 9.0	0.38 – 0.47	5.0 – 7.7

PR0628T1

Table 1. Main plasma parameters of the discharges from the multimachine database.

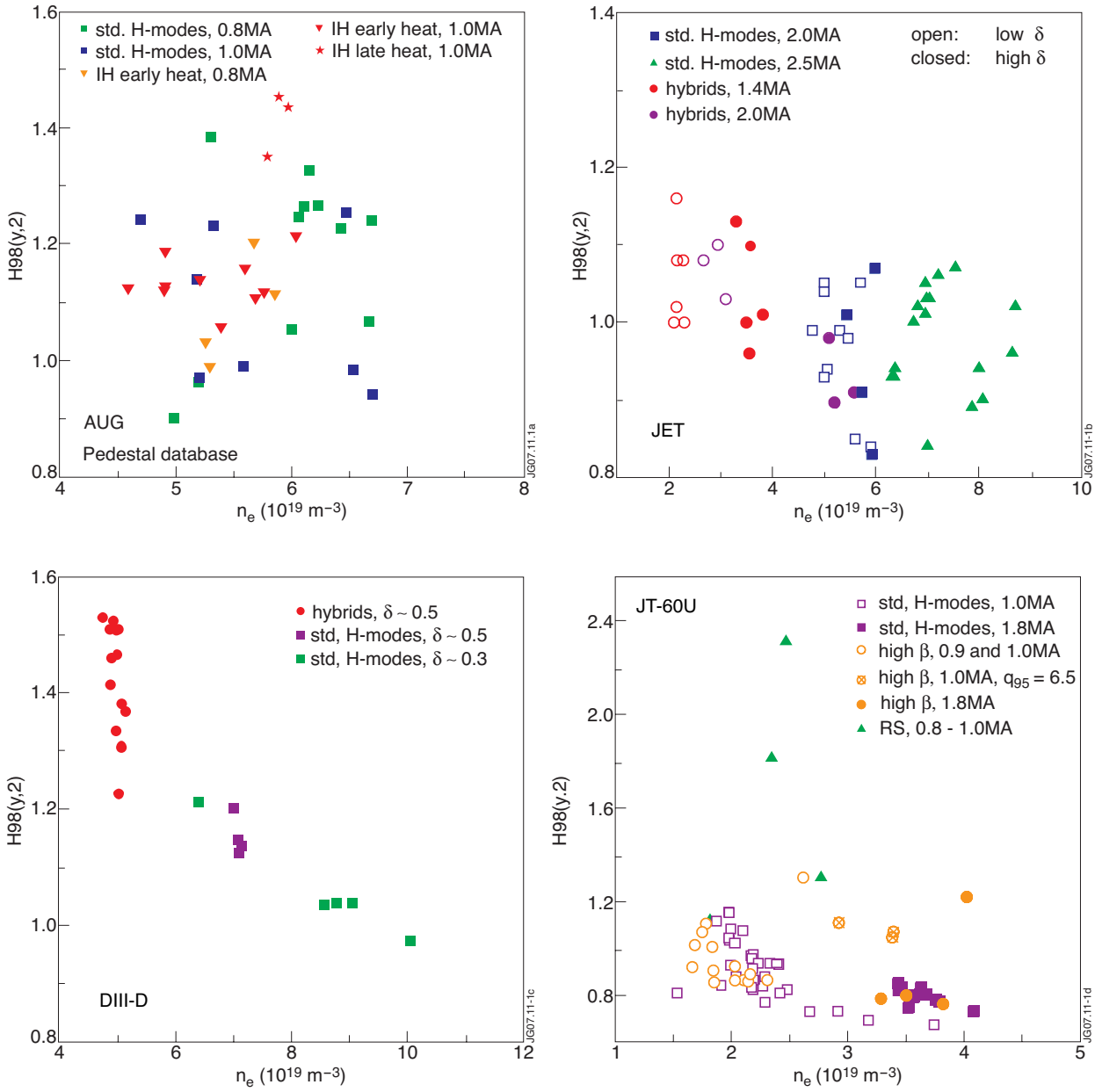

Figure 1: H98(y,2) versus line averaged density for the selected discharges from AUG, DIIID, JET and JT-60U.

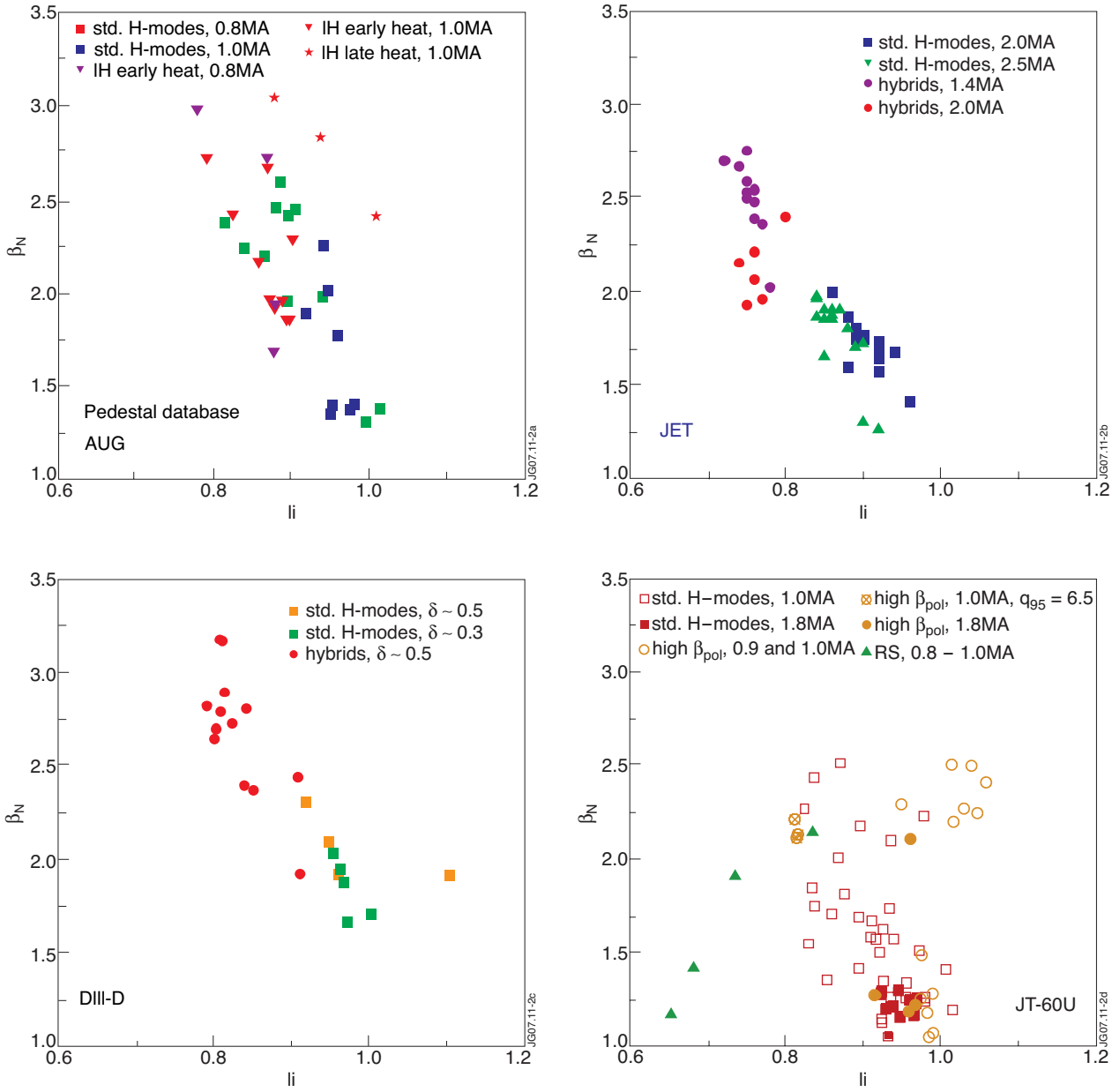

Figure 2: Total β_N versus li for the selected discharges from AUG, DIII-D, JET and JT-60U.

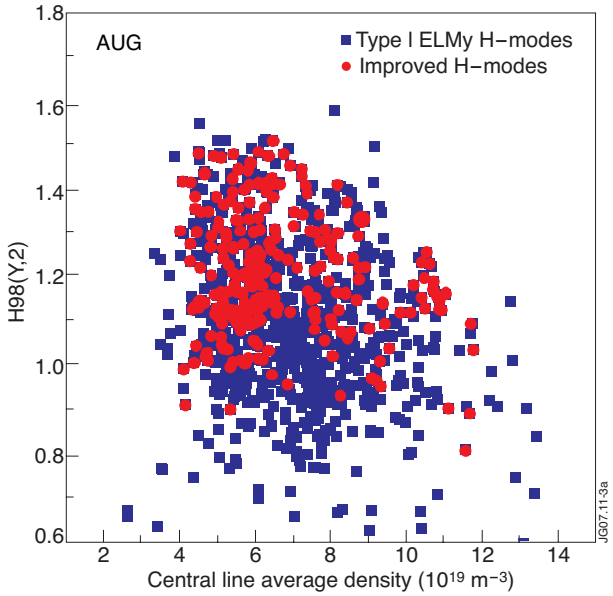

Figure 3a: H98(y,2) versus central line averaged density for AUG type I ELMy H-modes and the subset of improved H-modes, from ref. [21].

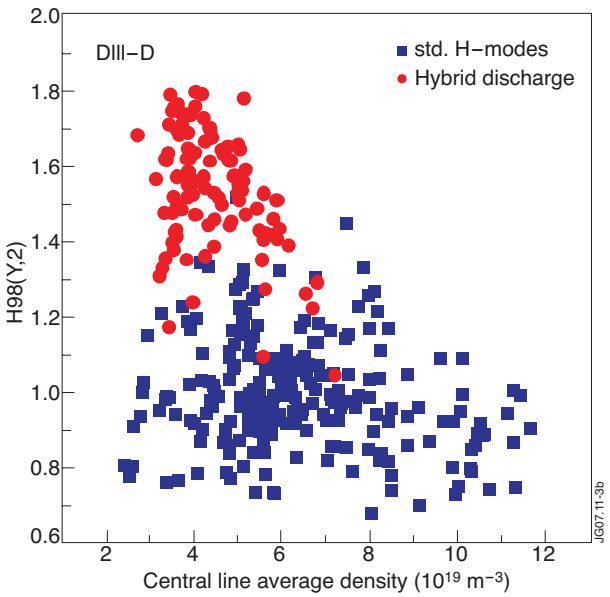

Figure 3b: H98(y,2) versus line averaged density for DIII-D conventional and hybrid ELMy H-mode discharges (courtesy of CDBM ITPA group).

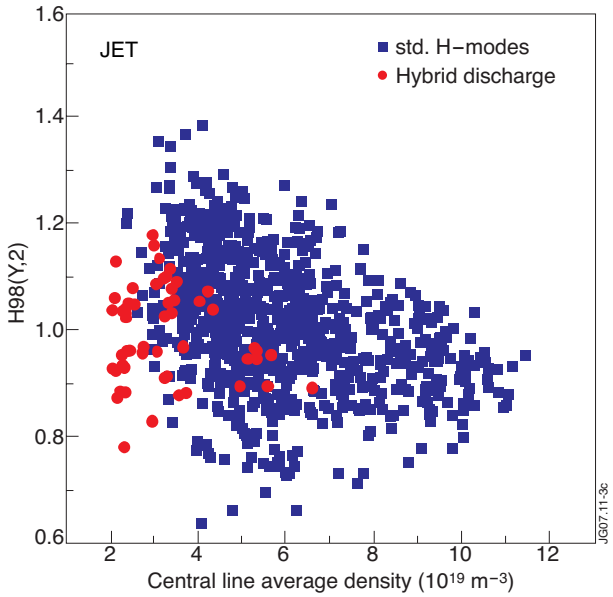

Figure 3c: H98(y,2) versus central line averaged density for JET ELMy H-modes, selected from the JET H-mode confinement database, and hybrid discharges (courtesy of CDBM ITPA group).

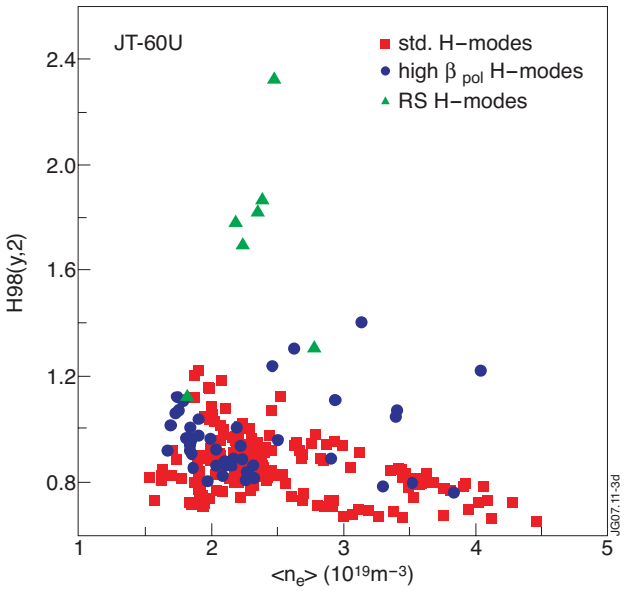

Figure 3d: H98(y,2) versus central line averaged density for JT-60U standard ELMy Hmodes, high β_{pol} discharges and Reversed Shear (RS) H-modes.

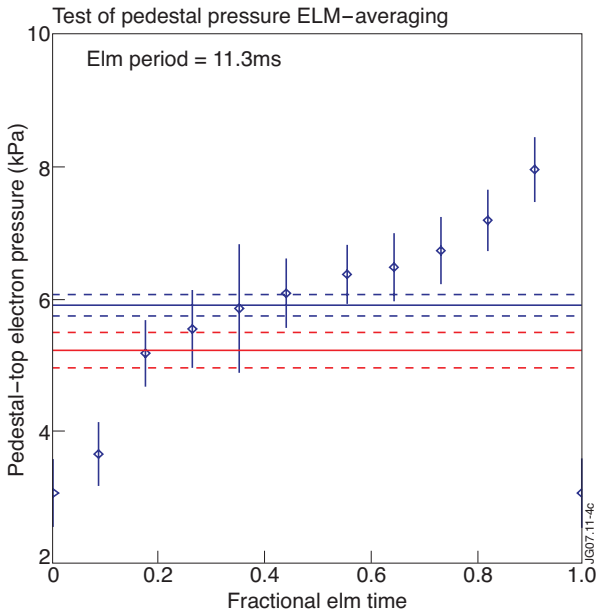

Figure 4: Evolution of pedestal top pressure during an ELM cycle (example from AUG): fit of p_e^{PED} from the entire ELM cycle (solid red line), p_e^{PED} fits at regular time intervals during the ELM cycle (blue diamonds) and their time average (solid blue line). The dashed lines represent the respective error bars.

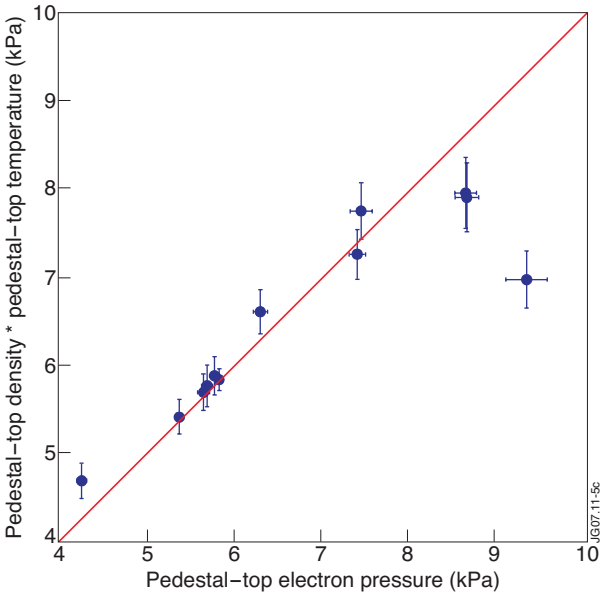

Figure 5: Comparison between electron pedestal top pressure derived directly from a mtanh fit of the electron pressure profile and that obtained from the product of pedestal top density and temperature. The example is from the DIII-D data set.

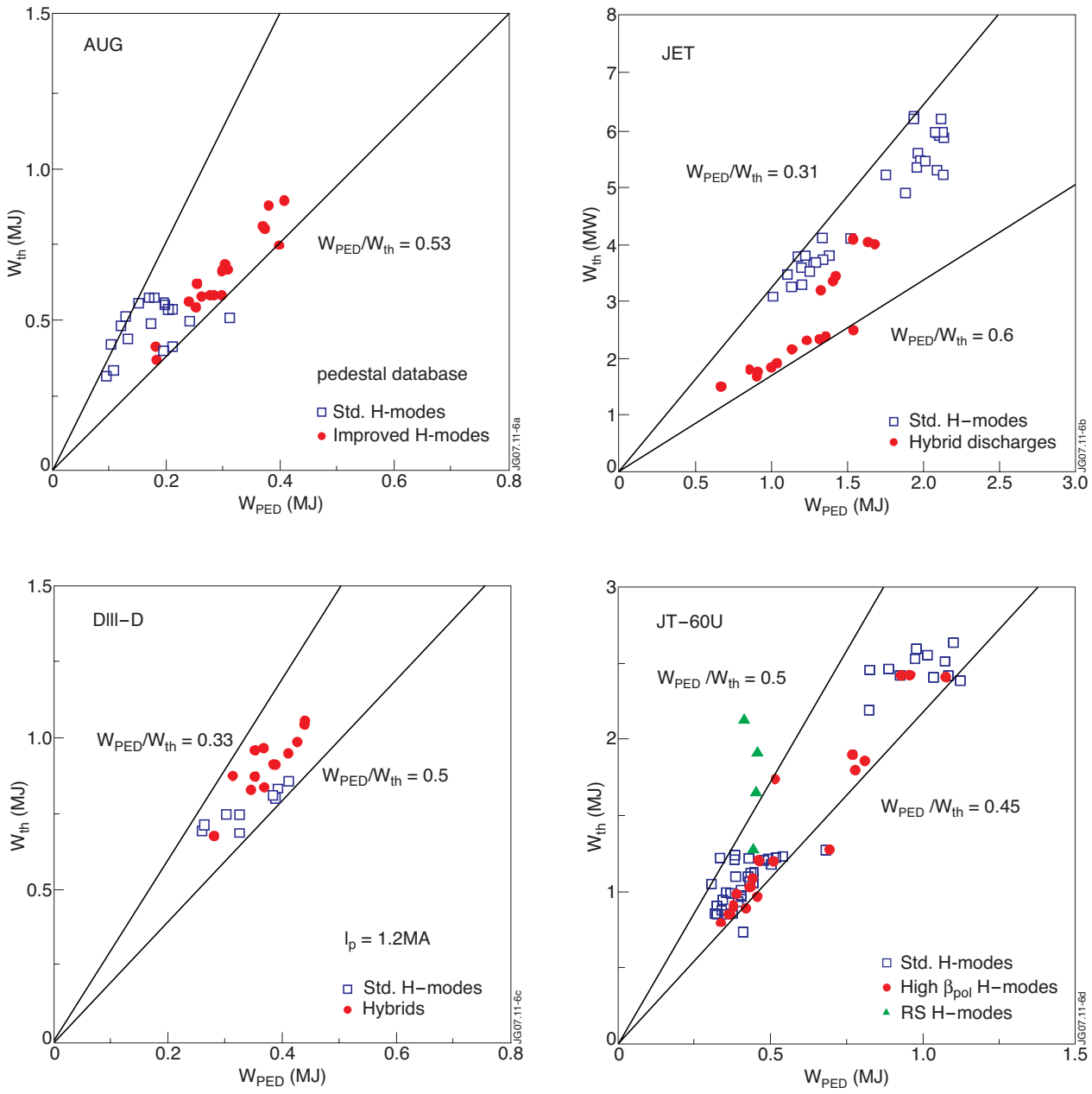

Figure 6: Thermal versus pedestal stored energy for AUG, DIII-D, JET and JT-60U.

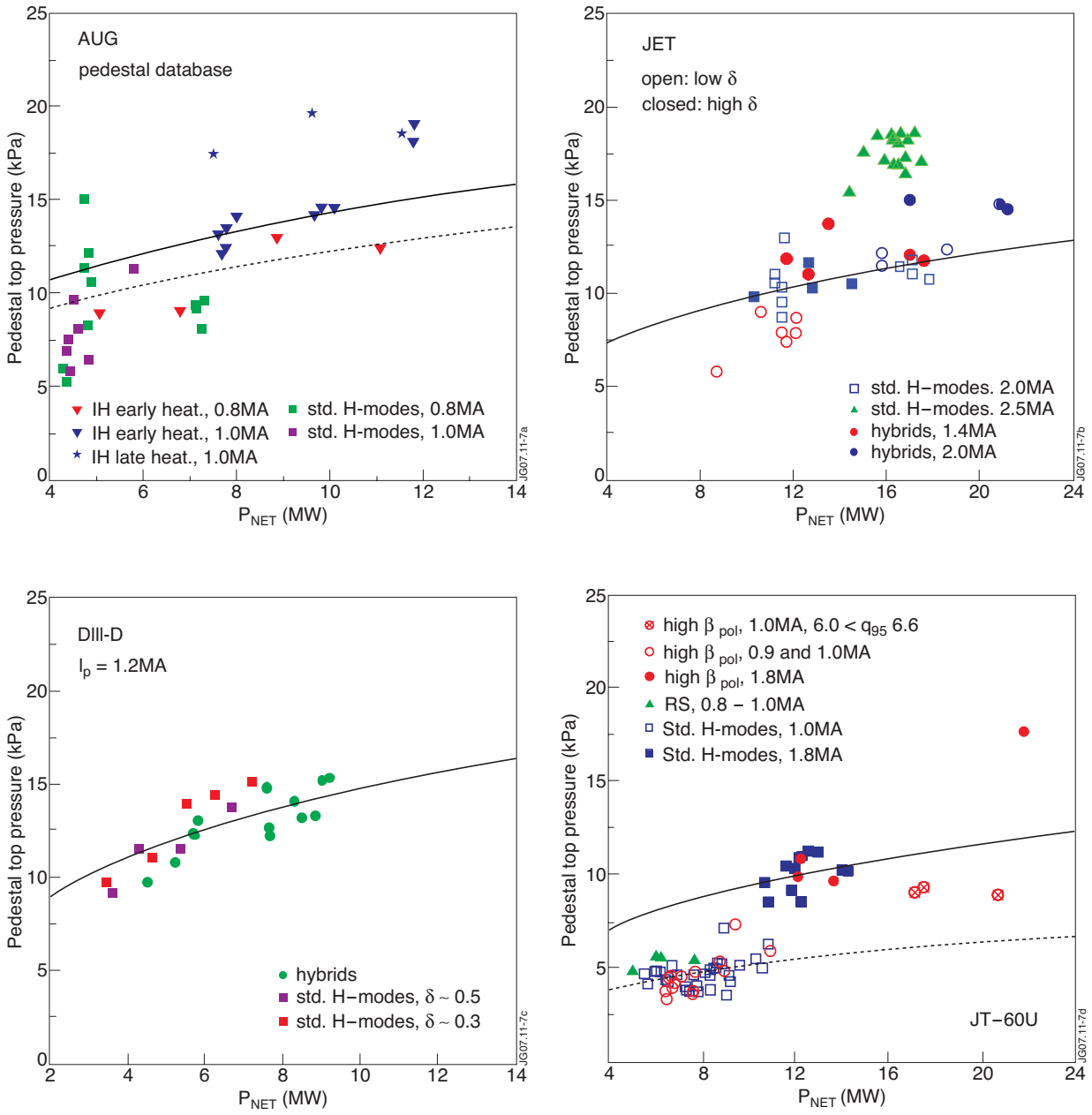

Figure 7: Pedestal top pressure versus net input power for AUG, DIII-D, JET and JT-60U.The lines are to guide the eye only along the curve $p^{PED} \sim P_{NET}{}^{0.3}$ *for each plasma current, namely following the power scaling of the IPB98(y,2) scaling expression.*

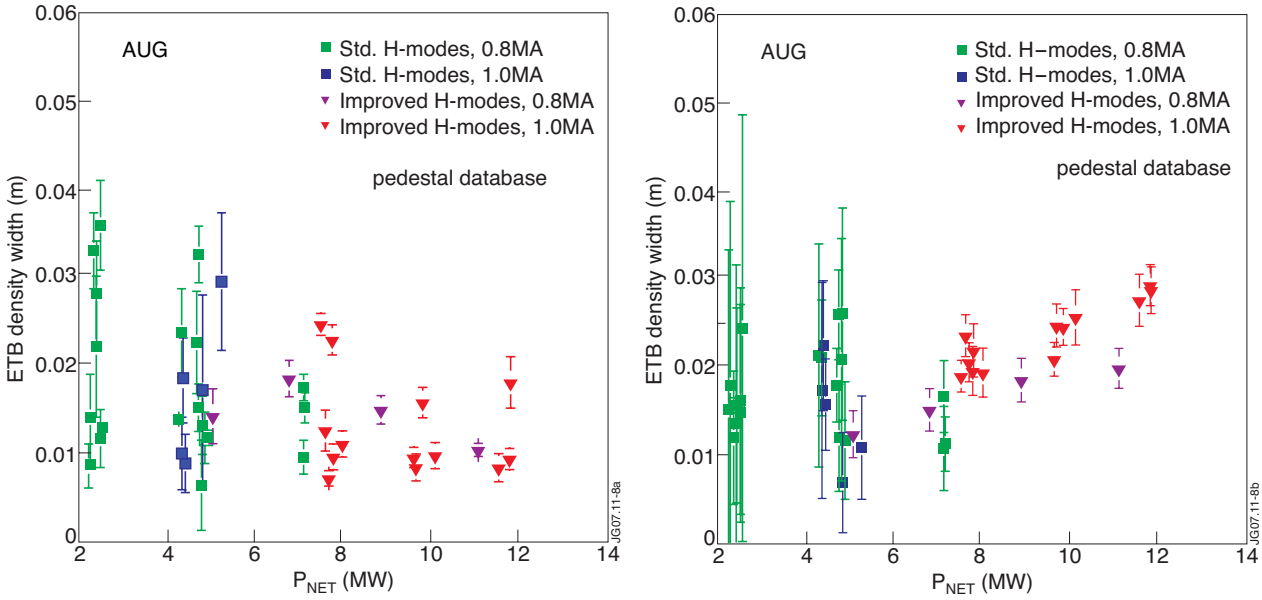

Figure 8: Variation of the electron density and temperature ETB widths with net input power for the AUG discharges.

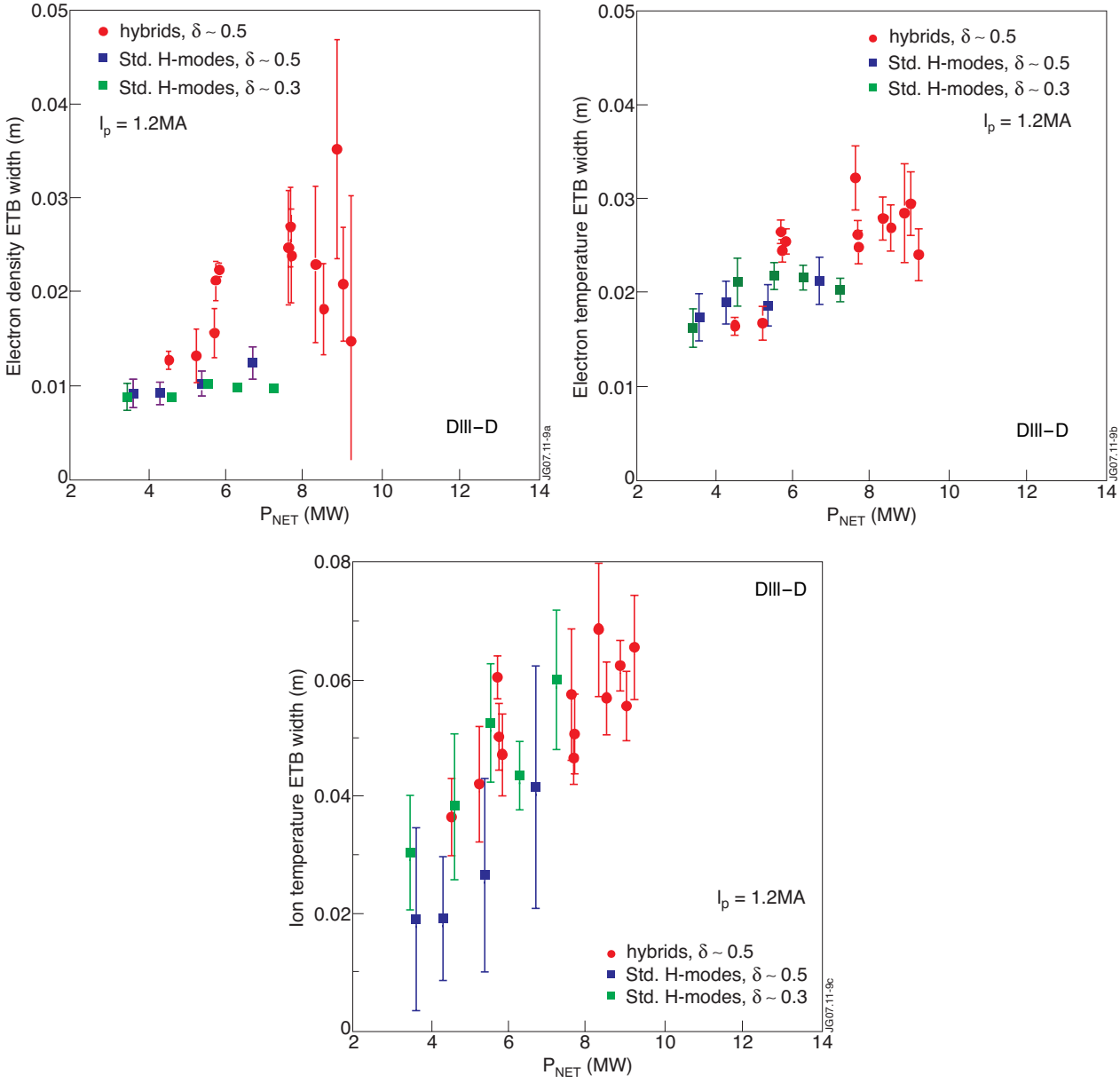

Figure 9: Variation of n_e, T_e and T_i ETB widths with net input power for the DIII-D discharges.

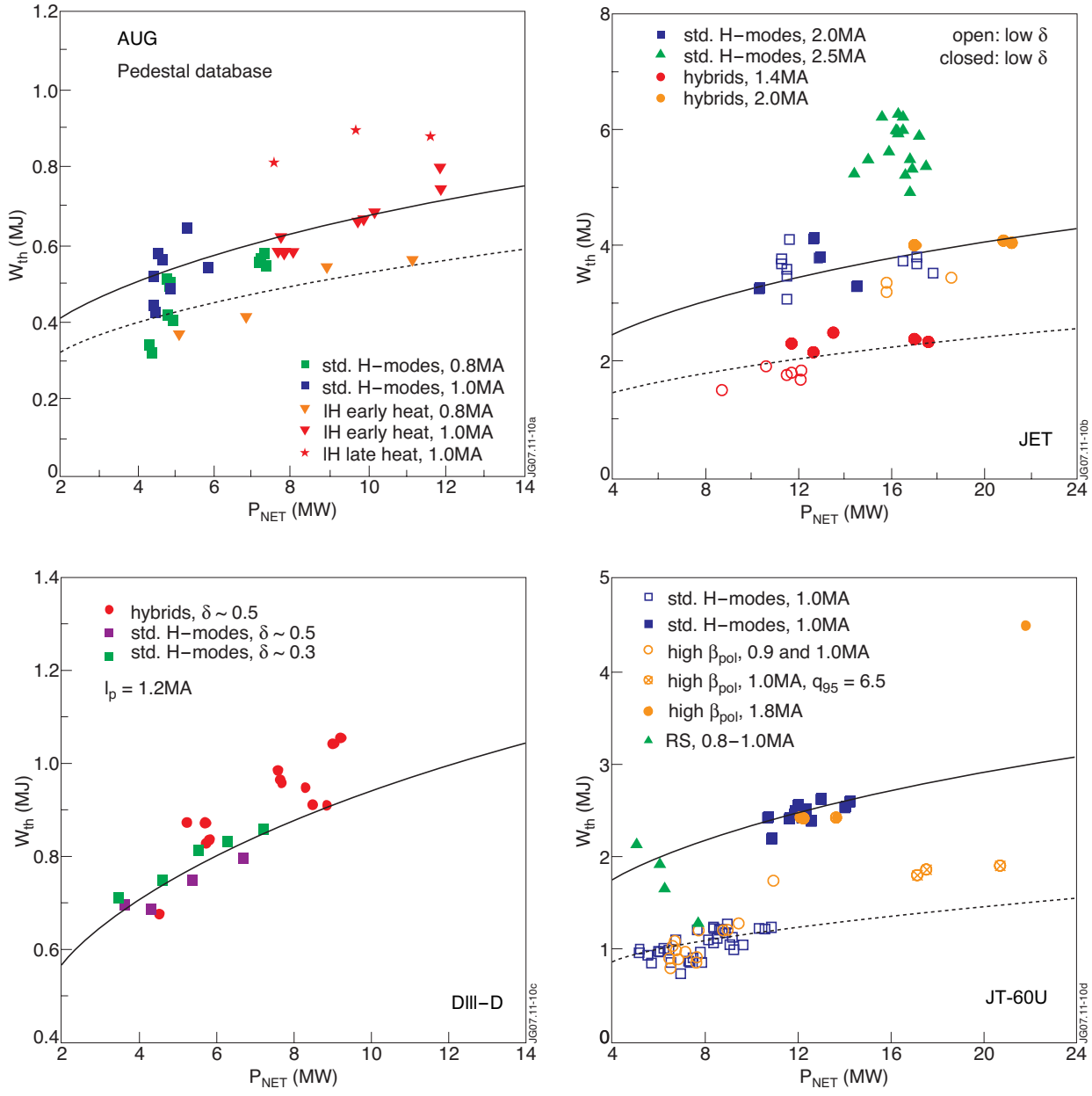

Figure 10: Total thermal stored energy versus net input power. The lines are to guide the eye only along the curve $W_{th} \sim P_{NET}^{0.31}$ *for each plasma current, namely following the power scaling of the IPB98(y,2) scaling expression.*

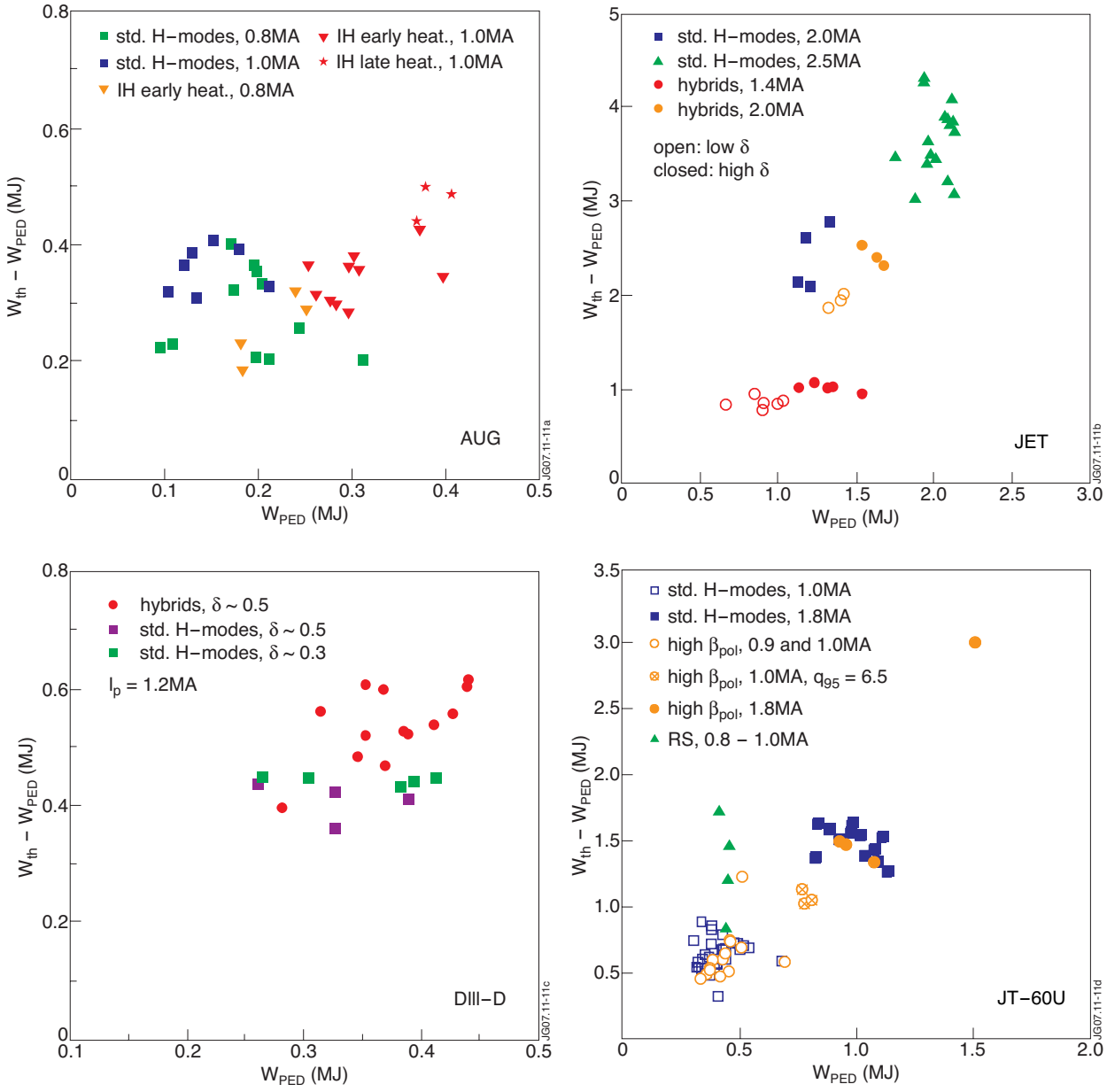

Figure 11: Core thermal stored energy versus pedestal stored energy.

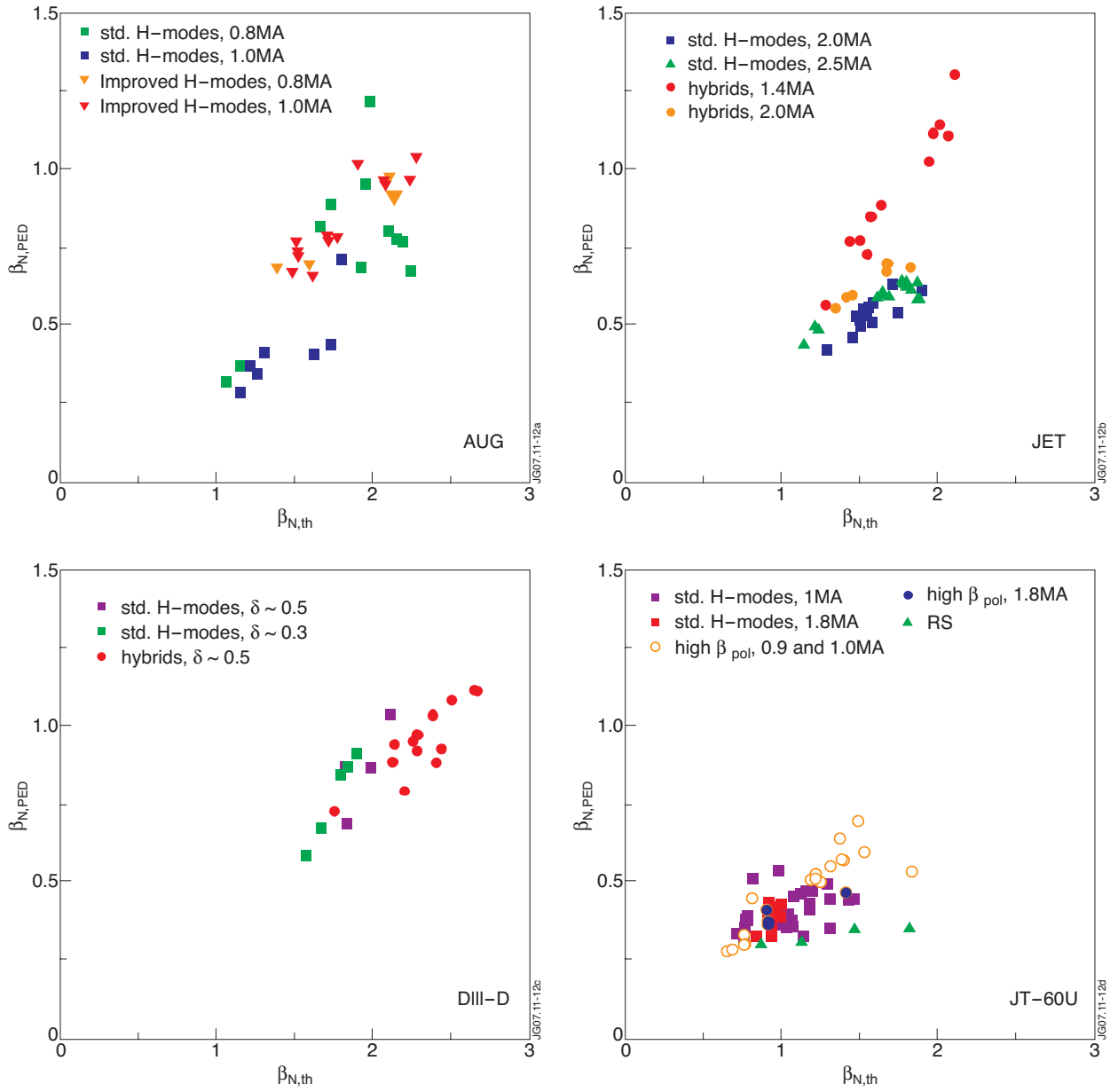

Figure 12: Pedestal β_N versus total thermal bN.

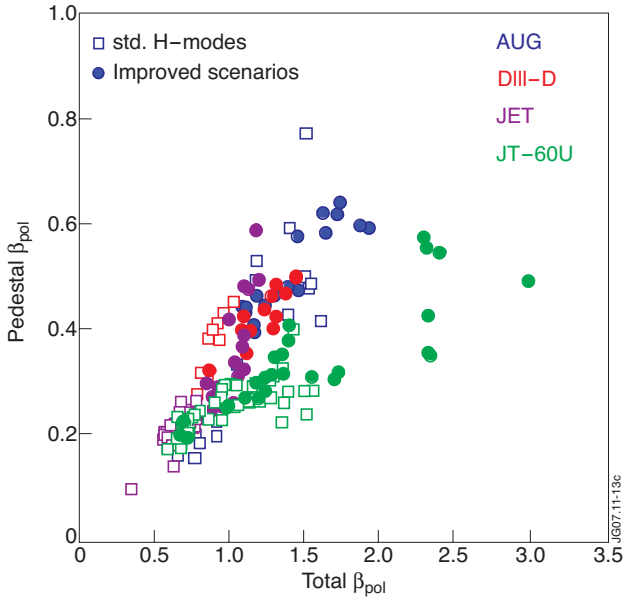

Figure 13: Pedestal β_{pol} versus total β_{pol}.

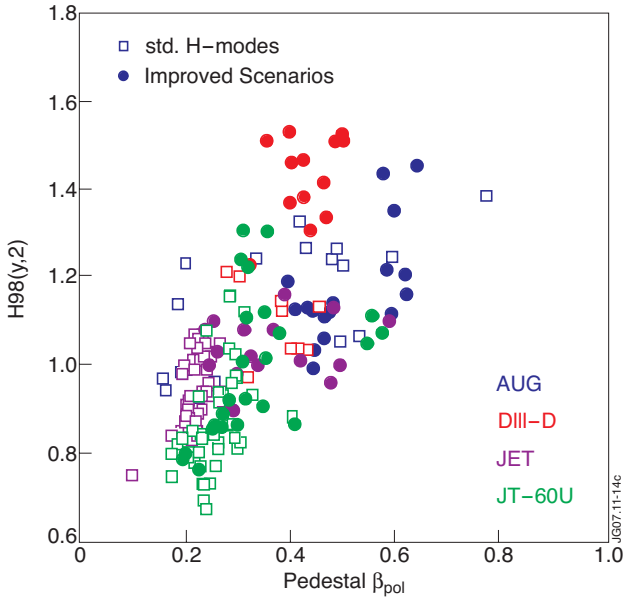

Figure 14: H98(y,2) factor versus pedestal β_{pol}.

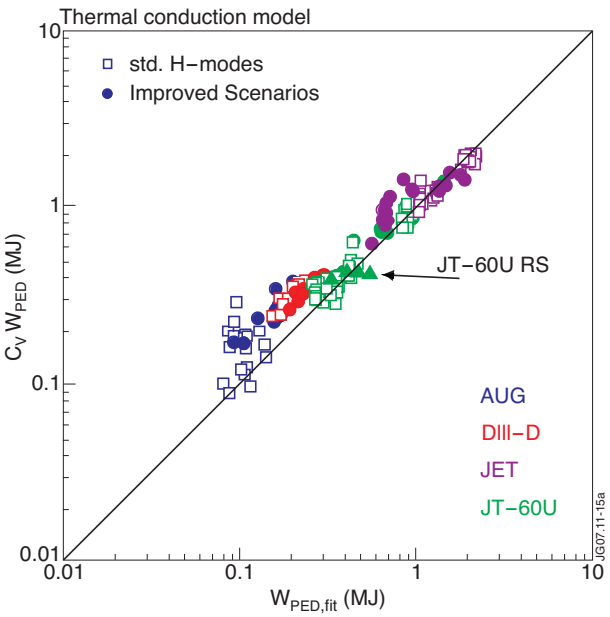

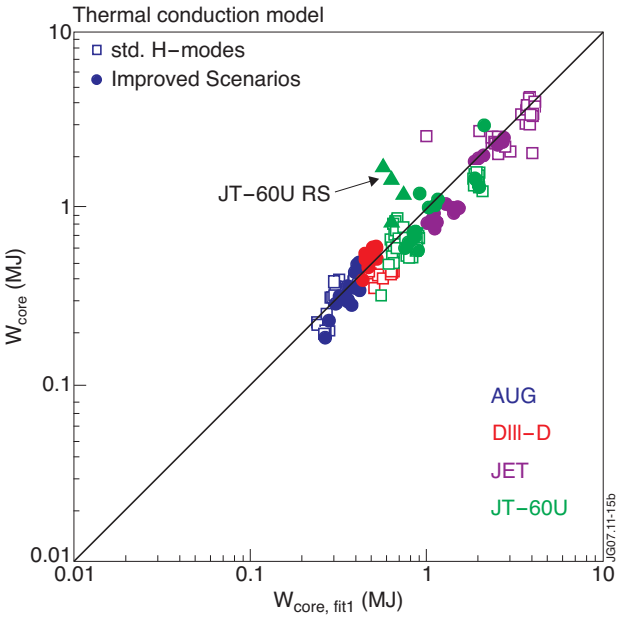

Figure 15: Cv W_{PED} versus the scaling expression $W^{PED,fit}$ for the thermal conduction model and W_{core} versus the scaling expression $W_{core,fit1}$ from eq (6) in [44].

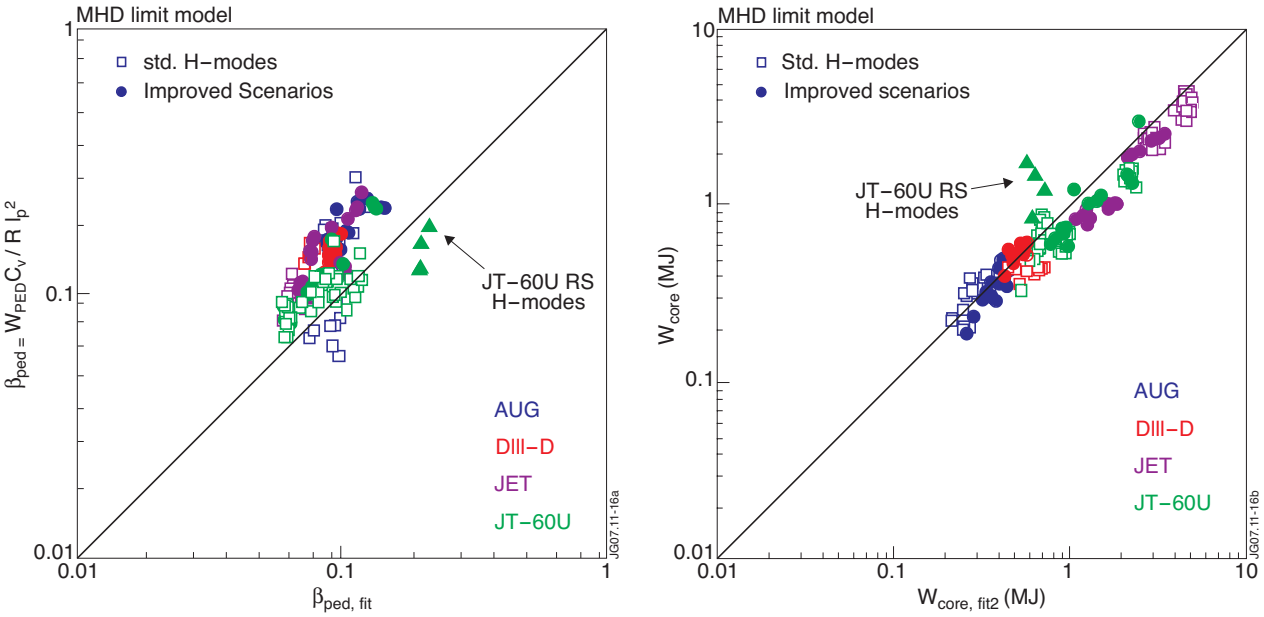

Figure 16: β_{ped} versus the scaling expression $\beta_{ped,fit}$ for the MHD limit model and W_{core} versus the scaling expression $W_{core,fit2}$ from eq (8) in [44].